www.apcc21.org

APCC TECHNICAL REPORT 2011-01

APCC
APEC CLIMATE CENTER

TECHNICAL REPORT

APCC
APEC CLIMATE CENTER

PREFACE

It is our pleasure to present to you the APEC Climate Center (APCC)'s Technical Report 2011, which reports the core outcomes of our research activities from the past year.

Since 2005, APCC, as a hub of climate information in the Asia-Pacific region, has strived to share our analysis and prediction of abnormal climate and to apply this information to regional development. The center has established the largest Multi-Model Ensemble (MME) system for seasonal prediction through its international science network and has provided value-added products to various stakeholders. Recently, APCC has expanded its mandate to include enhancement of the capacity of APEC member economies information to respond effectively to climate change and variability through better application of climate.

To achieve its research and social objectives, in 2011, APCC made efforts to research improvements in its climate prediction performance from various angles and towards better understanding of climate variability and the reproducibility of the climate models for the relevant application of climate information to society. The following technical report provides more information about our research outcomes from 2011.

APCC will continue to improve the quality and accuracy of climate information, recognizing that the utility of this information is only as good as its quality. We would like to make the best use of our research results for the benefit of society and academia. We also welcome any feedback on this report or on our services.

My best and warmest regards to all of you.

Dr. Chin-Seung Chung
Director/APEC Climate Center

CONTENTS

Reduction Biases in Regional Climate Downscaling: Application of Bayesian Model Averaging on the Large-Scale Forcing

Dr. Hongwei Yang

APCC
TECHNICAL REPORT 2011-01

Reduction Biases in Regional Climate Downscaling:

Application of Bayesian Model Averaging on the Large-Scale Forcing

Dr. Hongwei Yang

ABSTRACT

Simulations of the 1998 East Asian summer monsoon were carried out using the Weather Research and Forecast (WRF) model forced by four reanalysis datasets (NCEP-R2, ERA-40, ERA-IN, and JRA-25), their equally weighted ensemble mean, and their ensemble mean based on Bayesian model averaging (BMA). Large discrepancies were found among experiments forced by individual reanalysis datasets. The uncertainties in the moisture field of large-scale forcing over ocean were responsible for the discrepancies. The control experiment forced by the equally weighted ensemble forcing reduced the biases in simulated circulation to a large extent, but only reduced the biases in simulated precipitation in some cases. The experiment forced by the BMA ensemble forcing outperformed not only the experiments forced by individual reanalysis datasets but also the control experiment. The results suggest that the uncertainties in lateral boundary forcing can be reduced through the BMA ensemble method based on the satellite data, and that more and improved three-dimensional satellite data is urgently demanded.

1. Introduction

Since the first demonstrations of regional climate model (RCM) by Dickinson et al. (1989) and Giorgi and Bates (1989), the applications of RCM, such as climate downscaling, sensitivity study, and regional ecosystem assessment, etc., have rapidly developed to meet the great demands from society. Evaluating uncertainties in regional climate modeling is becoming increasingly important. Thus meteorologists are trying to identify the bottom line of the uncertainties of RCMs and the sources of the systematic errors.

A number of inter-comparison projects of regional model have been carried out to make people to identify common model strengths and weaknesses over specific regions such as Europe (Christensen et al. 1997), the United States of America (Takle et al. 1999; Curry and Lynch 2002; Anderson et al. 2003; Mearns 2004), and East Asia (Leung and Ghan 1999; Fu et al. 2005), COordinated Regional climate Downscaling Experiment (García-Díez et al. 2011; Fernández et al. 2010) which is sponsored by World Climate Research Programme to produce regional climate change scenarios globally, contributing to the Intergovernmental Panel on Climate Change (IPCC) AR5 and to the climate community beyond the AR5, and the regional climate models studies in the West African Monsoon Modeling and Evaluation (Druyan et al. 2009). Many studies showed that RCMs even driven by analysis datasets could produce biases in seasonal or monthly averaged surface air temperature and precipitation (IPCC, 2001). The biases in surface air temperature and in precipitation are generally below 2°C and within 5 to 50%, respectively (Giorgi and Mearns, 1999; Giorgi and Shields, 1999; Small et al. 1999a,b; van Lipzig, 1999; Pan et al. 2001), which can be especially high over remote areas or mountainous regions.

Being as an initial boundary value problem, three sources of the biases are introduced into RCM simulation: uncertainties from initial condition, biases of the lateral boundary forcing, and the uncertainties introduced by the internal variabilities of the model itself. The main purpose of this paper is to investigate the sensitivity of RCMs to the uncertainties in the lateral boundary forcing, while study of the uncertainties come from the initial condition and model internal variabilities is beyond the present scope of this study.

Numerous studies demonstrate that the uncertainties in a nested RCM are mainly coming from the lateral boundary forcing that is used to drive the simulation (e.g., Giorgi and Bi 2000; Liang et al. 2001, 2004; Diaconescu et al. 2007; Gong and Wang 2000; Dimitrijevic and Laprise 2005; Miyakoda and Rosati 1977; Anthes et al. 1985; Gustafsson 2002; Mohanty et al. 1990; Jacob and Podzun 1997; Paegle et al. 1997; Pan et al. 2001; Denis et al. 2002; Wu et al. 2005; Zhong 2006; Qian and Liu 2001; Noguer et al. 1998). The uncertainties induced by the lateral boundary forcing persistently influence the RCM simulation through the entire integration (Anthes et al. 1985). Giorgi and Bi (2000) showed that the random perturbation of the lateral boundary forcing grew during the earlier stage of 5 to 15 days, and then the motions reached a dynamic equilibrium controlled by the internal model variability, which was determined by the meteorological regimes, rather than by the perturbation itself. They demonstrated that generally in long-term simulations, the uncertainties of the initial condition dominated the response of RCM in the early stage and the biases of the lateral boundary condition would dominate the later stage of the simulation when the lateral boundary information pervaded the interior of the domain. Paegle et al. (1997) showed that the small perturbation of large scale is more important than the small perturbation of small scale to the development of small scale motions, which actually agrees with the findings of Thompson (1957) and Lorenz (1969). They indicated that the uncertainties of large scale induced the uncertainties of lateral boundary forcing, which thus is more important than the small perturbation of local initial condition. So the uncertainties induced by the lateral boundary forcing are generally larger than those induced by the initial condition, model resolution, physical parameterizations, domain size (Vukicevic and Errico 1990; Jacob et al. 1997; Elía et al. 2008), and even the RCM used (Arritt and Rummukainen 2011).

Moreover, various responses of the RCM to the uncertainties in lateral boundary forcing have been observed. Wu et al. (2005) found the biases in the lateral boundary forcing generally contributed more to the overall uncertainties than that produced by the biases in the initial condition and no clear trend was observed on the evolution of the uncertainties on the lateral boundary forcing, whereas Christensen et al. (1997) found the RCM amplifies the biases in lateral boundary forcing. However Hong et al. (1999) found the RCM reduces the biases.

Some studies focused on the impacts of domain sizes (Jones et al. 1995; Bhaskaran et al. 1996) and consistency between the driving GCM and driven RCM (Beniston et al. 2007). Other studies tried to reduce the influence of the uncertainties in lateral boundary forcing on RCM simulation. Qian and Liu (2001) found that choosing the lateral boundary location where the lateral boundary forcing has rather small biases improves the performance of the RCM. Xue et al. (2007) found that the RCM is sensitive to its southern lateral boundary condition when the buffer zone is extended to the tropics and is able to obtain the reasonable simulations only with when an appropriate lateral boundary location is selected. Similarly, Liang et al. (2001) found there is large discrepancy in atmospherical humidity between the National Centers for Environmental Prediction–National Center for Atmospheric Research global reanalysis datasets (Kalnay et al. 1996) and the ERA-40 reanalysis datasets over the lower latitude, and suggested that the lateral boundary location should be chosen to avoid this area.

However, none of the studies tried to directly decrease the uncertainties in lateral boundary forcing. In the simulations of the East Asian summer monsoon, Wang and

Yang (2008; figure 1) and Yang et al. (2011; figure 2) found that the Weather Research and Forecast (WRF) model driven by the ERA-40, National Center for Environmental Prediction-Department of Energy reanalysis data (NCEP-R2), and the Japanese 25-year reanalysis (JRA-25) yields different results. All experiments have significant deficiencies in reproducing the observed rainfall and have large biases in simulating the atmospheric circulation. The authors found that the large vapor uncertainties among reanalysis datasets over the Bay of Bengal and the Philippine Sea are the key factor that induces the largely different realizations. The equally weighted ensemble forcing lessens the uncertainties in lateral boundary forcing and therefore improves the performance of the model.

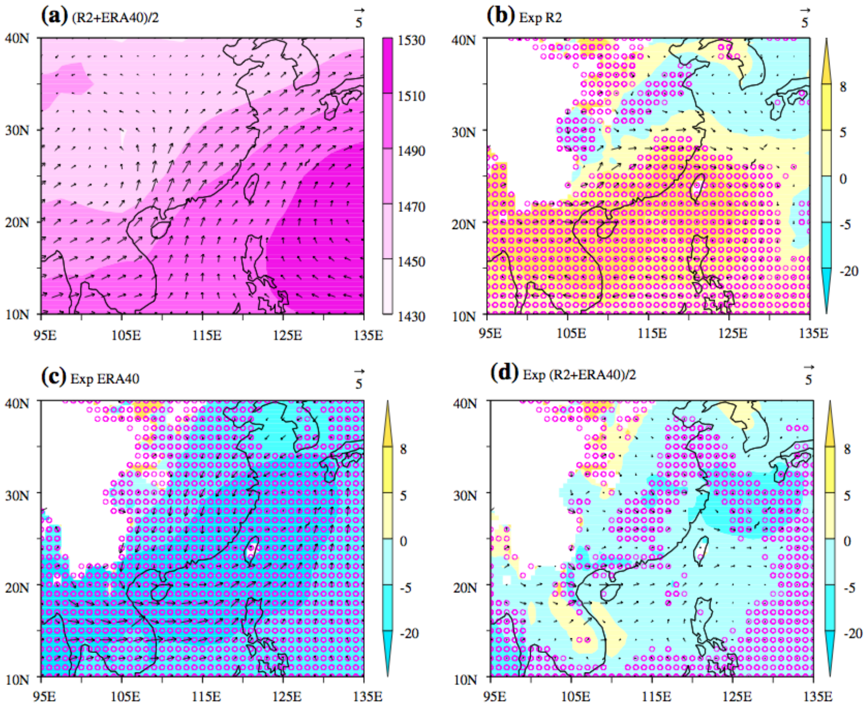

Figure 1 (a) Summer June–July–August (JJA) mean geopotential height (shading in units of meter) and horizontal winds (vector in units of ms^{-1}) at 850 hPa that are derived from the ensemble mean of NCEP-R2 and ERA-40 reanalysis data. Shown in (b), (c) and (d) are the WRF model biases that were simulated with lateral boundary conditions derived from (b) NCEP/DOE reanalysis 2 (NCEP-R2), (c) ECMWF reanalysis (ERA-40), and (d) ensemble mean of ERA-40 and NCEP-R2 control, respectively. All the biases are defined by the departure of RCM simulations from the ensemble mean of NCEP-R2 and ERA-40. The purple circles indicate the significant areas with 99% confidence level in the difference of geopotential height by t test

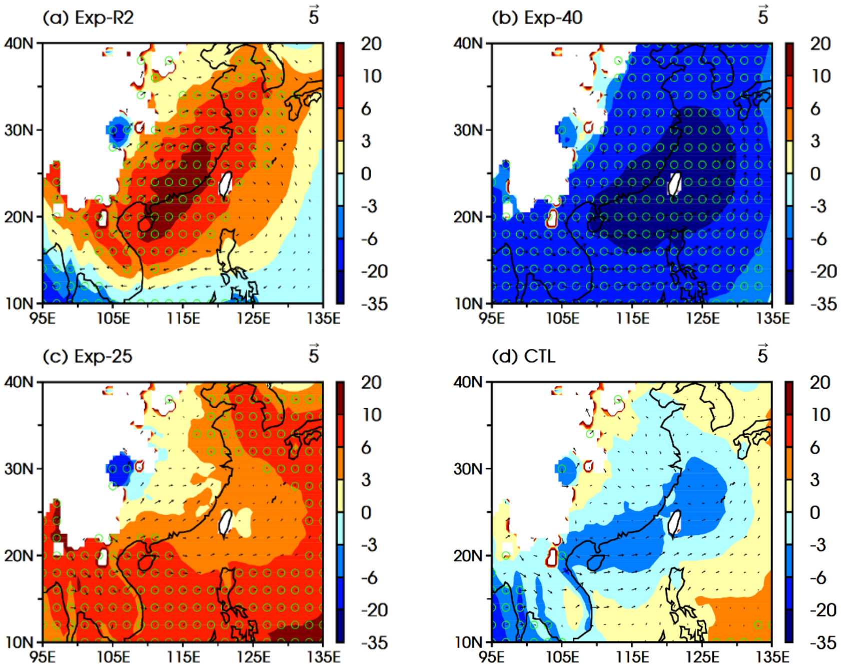

Figure 2 The WRF model biases on geopotential height (shading in units of meter) and horizontal winds (vector in units of ms^{-1}) at 850 hPa in climate summer June–July–August (JJA). Respectively, (a), (b), (c) and (d) are the biases that were simulated with lateral boundary conditions derived from (a) NCEP/DOE reanalysis 2 (NCEP-R2), (b) ECMWF 40-year reanalysis (ERA-40), (c) the Japanese 25-year reanalysis (JRA-25), and (d) the ensemble mean of the three reanalysis datasets. All the biases are defined by the departure of RCM simulations from the corresponding large-scale forcing. The green circles indicate the significant areas with 95% confidence level in the difference of geopotential height by t-test.

However, the experiments in Wang and Yang (2008) and Yang et al. (2011) were driven by the equally weighted ensemble forcing and did not consider the specificity of different reanalysis datasets, especially the characteristic of humidity fields that induce the large model biases. The optimized ensemble scheme is more competent than the equally weighted ensemble method when the models are very different (Arritt and Rummukainen 2010). Recently, the optimized ensemble method of Bayesian model averaging (BMA) (Hoeting et al. 1999) was being increasingly used in ensemble prediction (Raftery et al. 2005; Sloughter et al. 2007), climate change projection (Min and Hense 2006), and hydrology prediction studies (Duan et al. 2007). The BMA ensemble mean is a weighted average of the ensemble members. The weights are estimated according to the performance of individual members on simulating the given training data. Thus, we are motivated using the BMA method to the key field, i.e. the humidity field which has the leading uncertainties among the variables in lateral boundary forcing, in order to investigate the efficient ways to reduce the model biases. We want to address the following questions: Does the BMA ensemble forcing effectively reduce the model biases? Can the BMA ensemble forcing further improve the RCM performance than the equally weighted ensemble forcing does?

To answer the questions, we simulate the 1998 East Asian summer monsoon with WRF model driven by NCEP-R2, ERA-40, JRA-25, the third generation ECMWF reanalysis product INTERIM (ERA-IN), as well as their equally weighted ensemble mean, and the same forcing of the previous one except that the humidity field is developed by the BMA method. The model and data are described in Section 2. The experiments are designed in Section 3. Section 4 presents biases in the experiments driven by individual reanalysis datasets. The source of the model biases are discussed in Section 5. In Section 6, we describe the application of the BMA method. Section 7 shows the performance of experiments forced by the equally weighted ensemble forcing and the BMA ensemble forcing. Section 8 is the discussion and the final section presents the summary and conclusion.

2. Model and data

The Weather Research and Forecast (WRF) model (Skamarock et al. 2005) a primitive equation model under sigma coordinates, is used in this study. WRF is a next-generation regional prediction and downscaling system designed to meet both operational forecasting and atmospheric research needs. It has a advanced software architecture allowing for parallel computing and system extensibility. The development of the state of the art WRF has been a collaborative partnership, mainly among the National Center for Atmospheric Research, the Forecast Systems Laboratory, the National Oceanic and Atmospheric Administration, National Centers for Environmental Prediction, the Air Force Weather Agency, the Naval Research

Laboratory, the University of Oklahoma, and the Federal Aviation Administration. WRF allows researchers the ability to conduct simulations reflecting either real data or idealized configurations. WRF is suitable for many applications of different scales ranging from meters to thousands of kilometers. Such applications include research and operational numerical weather prediction (NWP), data assimilation and parameterized-physics research, downscaling climate simulations, driving air quality models, atmosphere-ocean coupling, and idealized simulations (e.g. boundary-layer eddies, convection, baroclinic waves).

There are two dynamics solvers in the WRF Software Framework (WSF): the Advanced Research WRF (ARW) solver (originally referred to as the Eulerian mass or "em" solver) developed primarily at NCAR, and the NMM (Nonhydrostatic Mesoscale Model) solver developed at NCEP. We chose the ARW solver in this study. The governing equations of the ARW dynamics solver are the compressible, nonhydrostatic Euler equations. The equations are written in flux form with variables have conservation properties, following the philosophy of Ooyama (1990). And, the equations are expressed by using a terrain-following mass vertical coordinate (Laprise, 1992). The top of the model is a constant pressure surface, for which 50mb pressure surface is used in this study. Horizontal Grid uses Arakawa C-grid staggering. Time-split integration uses a 3rd order Runge-Kutta scheme with smaller time step for acoustic and gravity-wave modes (Klemp and Wilhelmson 1978; Skamarock and Klemp 1992; Wicker and Skamarock 2002).

WRF offers multiple physical options that can be combined in any way (Skamarock et al. 2005). In our study, we choose Purdue Lin scheme as the microphysics parameterization which includes six types of hydrometeors: water vapor, cloud water, rain, cloud ice, snow, and graupel. All parameterization production terms are based on Lin et al. (1983), Rutledge and Hobbs (1984), and Tao et al. (1989). Detailed description can be found in Chen and Sun (2002).

We choose Betts-Miller-Janjic (Janjic 1994; 2000) scheme as the cumulus parameterization which was derived from the Betts-Miller (BM) convective adjustment scheme (Betts 1986; Betts and Miller 1986) with several different important aspects (Janjic 2000).

The surface layer scheme adopts stability functions from Paulson (1970), Dyer and Hicks (1970), and Webb (1970) to calculate surface exchange coefficients for heat, moisture, and momentum.

Land surface parameterization is the Noah LSM scheme which was developed jointly by NCAR and NCEP. This is a 4-layer soil temperature and moisture model with canopy moisture, snow cover, and soil ice prediction. Details of the OSU LSM are described by Chen and Dudhia (2001).

The Yonsei University (YSU) PBL is employed here, which uses the counter gradient terms to represent fluxes due to non-local gradients.

Long wave Rapid Radiative Transfer Model (RRTM) is chosen in this study. RRTM is based on Mlawer et al. (1997) and is a spectral-band scheme using the correlated-k method. RRTM uses pre-set tables to represent accurately long wave processes due to water vapor, ozone, CO2, trace gases, and cloud optical depth.

Dudhia (1989) shortwave scheme is used in this study, which considers clear-air scattering, water vapor absorption (Lacis and Hansen 1974), cloud albedo, and absorption. It uses look-up tables for clouds from Stephens (1978).

Four reanalysis datasets were used as the large-scale forcing fields: NCEP-R2 (Kanamitsu et al. 2002), ERA-40 (Uppala et al. 2005), ERA-IN (Dee et al. 2011), and JRA-25 (Onogi et al. 2007). The lateral boundary forcing fields were geopotential height, air temperature, specific humidity, and horizontal winds. The width of the buffer zone in our model was set to be 10 grid points, where the prognostic variables of WRF model were nudged toward the reanalysis fields following the method of Davies and Turner (1977) with Newtonian nudging and horizontal diffusion within the RCM buffer zones. The initial state consists of surface pressure, sea-level pressure, 2-m height moisture, 2-m height temperature, 10-m height horizontal winds, soil moisture, soil temperature, and skin temperature. The skin temperature over the ocean was considered sea surface temperature. Horizontal resolution of thirty-second topography and land use data in Noah LSM is from the U.S. Geological Survey. The thirty-second soil type data is deduced from the State Soil Geographic (STATSGO) Database and five-minute global data from the Food and Agriculture Organization of the United Nations.

The water vapor path of the Hamburg Ocean Atmosphere Parameters and Fluxes from Satellite Data (HOAPS-3; Andersson et al. 2007) was used as the observed training data to validate the humidity fields of the reanalysis datasets in the BMA method. This data is globally gridded multi-satellite composite products with spatial and temporal resolution of 1 degree and 12 hours, respectively. Each grid-cell contains data from only one satellite with no multi-satellite averaging. Early passes are overwritten by later passes. This method provides more spatial homogeneity than averaging all available data. The fields are stored for 0-12 and 12-24 UTC. HOAPS-3 contains global precipitation and evaporation over the ocean and all basic state variables needed for the derivation of the fluxes. Almost all variables are derived from SSM/I passive microwave satellite data over the ice free global ocean. HOAPS-3 covers the time span from 07/1987 to 12/2005, resulting in a climatology containing 18 complete years of data.

The gauge-based Monsoon Asia Analysis precipitation with a resolution of 0.5° × 0.5° constructed by the Asian Precipitation–Highly–Resolved Observational Data Integration Towards Evaluation (APHRODITE) of the Water Resources project (Yatagai et al. 2009) was used to verify the simulated precipitation. The APHRODITE project develops state-of-the-art daily precipitation datasets with high-resolution grids for Asia. The datasets are created primarily with data obtained from a rain-gauge-observation network. The status of data collection and the domains are shown on the products page. In comparison with observed precipitation data, model results were interpolated into the grids of the observation data by using bilinear interpolation.

The simulated low-level wind fields and geopotential height were verified with the corresponding large-scale forcing reanalysis datasets.

3. Experimental designs

During the monsoon/meiyu-changma-baiu season in 1998, a extreme precipitation event occurred in the Yangtze River basin (26°-32°N, 103°-122°E; figure 3) that led to the worst flooding event in the recent 40 years, and, as a result, considerable impacts to the Chinese economics and society. This devastated event was associated with the extreme anomalous happened on the East Asia summer monsoon, as well as the impact of the strongest 1997/98 El Nino event in the last century (Ding and Liu 2001).

In 1998, westerlies first appeared over the South China Sea in middle May and then extended to the entire South China Sea, which indicates the onset of East Asian summer monsoon. From later May and early June, the monsoonal front moved northward and prevailed over south China. On around 10 June, the monsoon flow strengthened and rapidly moved to the Yangtze River basin and persisted there until the end of June. This normal meiyu event brought the first flood in the Yangtze River basin. Between late June and early July, the monsoon flow propagated farther north and the rainbelt moved to the Huaihe River basin. In middle and late July, the major rainbelt suddenly retreated to the Yangtze River basin again, which brought the unusual second meiyu caused severe floods over the Yangtze River basin in 1998.

Based on the event that we studied, we designed our model domain covering the East Asian summer monsoon region centered on 25°N, 115°E and extended from 5°N to 45°N and from 90°N to 140°E (figure 3). We choose Mercator map projection, thus the zonal grid space exactly equal to 0.5°, and the meridional grid space is almost 0.5° with a slight decrease from south to north. The model grid has a horizontal resolution of 50 km with 101 west-east and 92 south-north grid points, and 31 sigma layers in vertical direction up to 50 hPa.

There is distinct contrast between the topography over the northwest side of the domain and the land around the ocean. Low elevations are dominant throughout the east and south sides of the continent and maritime land, whereas elevations higher than 1.5 km are common in the northwest of the domain. The highest elevation, which is cut off by the west boundary of the domain between 25°N and 40°N, represents the Tibetan plateau which has the steepest slope located at its south and east side. Clay loam and regular loam are dominant soil types across East Asia. Grasslands and croplands occupy most of the area in the central China. Barren or sparsely vegetated land cover is located in the northwestern part of the domain. Forests are found in the northeastern part of the domain and in the southern flank of the Tibetan Plateau and Indochina. The low-level jet crossing the Bay of Bengal supplies abundant moisture to the East Asian summer monsoon region. The western North Pacific sub-tropical high residing in the Southeast dominates the evolution of monsoonal precipitation.

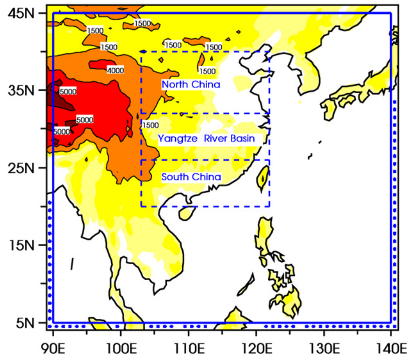

Figure 3 Simulation domain (enclosed by solid blue lines: 5°-45°N, 90°-140°E) and topography (color shading in units of meters). Topographic contours of 1500, 4000, and 5000 m are highlighted. The satellite-observed training data HOAPS-3 locates at the blue points outside the simulation domain. Analysis areas over land enclosed by dashed lines refer to South China (20°-26°N, 103°-122°E), the Yangtze River Basin (26°-32°N, 103°-122°E), and North China (32°-40°N, 103°-122°E).

Four sensitivity experiments named Exp-R2, Exp-40, Exp-IN, and Exp-25 were initially designed and, respectively forced by the NCEP-R2, ERA-40, ERA-IN, and JRA-25. The control experiment (CTL) was driven by the equally weighted ensemble mean of the four reanalysis datasets. To investigate the BMA method, we therefore designed another sensitivity experiment same as the CTL except the ensemble mean of the humidity fields was based on the BMA method and referred to it as Exp-BMA.

Generally, the reanalysis datasets NCEP-R2, ERA-40, and JRA-25 are available at 6-hour intervals with a horizontal resolution of 2.5° on an identical grid. To keep all sensitivity experiments and CTL in the same framework, we interpolated the ERA-IN through bilinear scheme from its original 1.5° grid to the 2.5° grid that the other reanalysis datasets sit on.

Since the NCEP-R2 and ERA-40 have only 17 pressure levels, we used the same levels from the ERA-IN and JRA-25 to maintain consistent vertical levels across the different datasets. Different from the ERA-40 and JRA-25, the surface data of ERA-IN and NCEP-R2 are 1.5° and 1.85° respectively, and were interpolated to 2.5° grid through bilinear scheme. So far all large-scale forcing had been prepared ready. The initial conditions of experiments Exp-R2, Exp-40, Exp-IN, and Exp-25 were taken from the NCEP-R2, ERA-40, ERA-IN, and JRA-25 reanalysis datasets, respectively. The same initial conditions of CTL and Exp-BMA were from the equally weighted ensemble mean of the four reanalysis datasets. The physical parameterization scheme and model configuration were kept the same for all experiments. All model parameters were taken with the default values without tuning.

All experiments were started from 00Z April 22 to 18Z August 31 in 1998. The days before May 1 were considered as a “spin-up” period (Giorgi and Mearns 1999) and the model output from May 1 to August 31 was analyzed. The spin-up time of 9 days may be insufficient for adjusting the atmosphere to land surface anomalies. Fortunately, the soil moisture-precipitation feedback is much less important than the moisture flux convergence anomaly during the Asian monsoon season (Douville et al. 2001).

4. Systematic biases forced by individual reanalysis datasets

The four sensitivity experiments forced by individual reanalysis datasets yielded different biases in simulations of the June-July-August (JJA) mean low-level 850-hPa circulations. Figures 4b, 4c, 4d, and 4e show the biases in 850-hPa circulations produced by Exp-R2, Exp-40, Exp-IN, and Exp-25, respectively. The biases were defined by the deviation of the RCM simulations from each corresponding forcing (e.g. the bias of Exp-R2 is the difference between Exp-R2 and NCEP-R2). The bias in Exp-R2 (figure 4b) was a notable anticyclonic high-pressure bias centered over Taiwan and spread over southeastern China along the adjoining oceanic region and over part of Indochina Peninsula. Exp-40 produced a bias (figure 4c) much larger than that in Exp-R2 but with an opposite sign: a cyclonic low-pressure bias occupied almost all the 850 hPa level centered over Taiwan island. Exp-IN (figure 4d) had a similar bias pattern of Exp-40 tilted north-east to south-west, but the range and the amplitude were smaller. Exp-25 (figure 4e) generated a high-pressure bias mainly over the Philippine Sea, the South China Sea, the Indochina Peninsula, and its associated circulations.

Further comparison of circulation between the model simulations and equally weighted ensemble mean of the four reanalysis datasets only showed a quantitative change (figure 5), because the circulation fields of the four reanalysis datasets were not considerable different much (see section 5 for details).

These different biases reflected the large uncertainties in experiments driven by individual reanalysis datasets. The location and strength of the western North Pacific subtropical high directly influences the East Asian summer monsoon. Therefore, the discrepancies would have marked effects on the monsoon precipitation in regional dynamic downscaling of the East Asian summer monsoon.

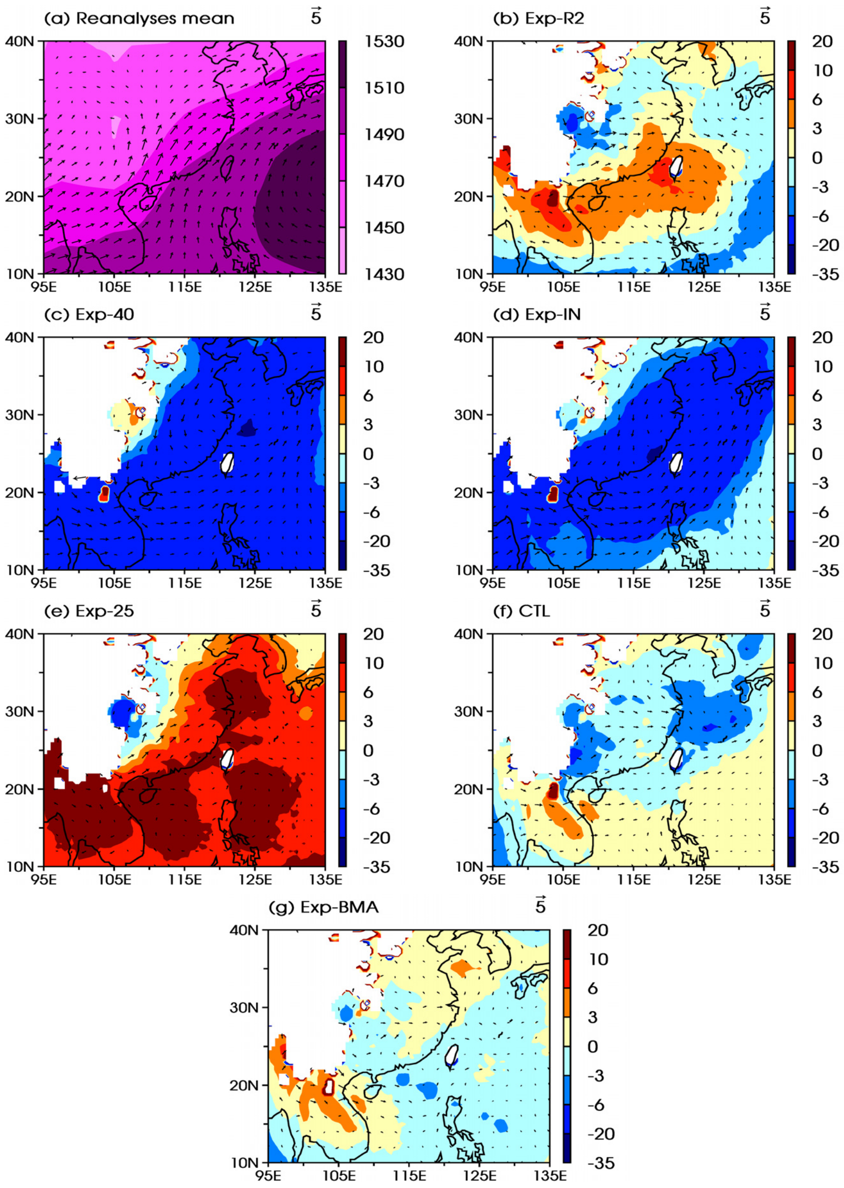

Figure 4 The model biases on geopotential height (shading in units of meter) and horizontal winds (vector in units of 5 ms^{-1}) at 850 hPa in summer (JJA) mean. Respectively, (b), (c), (d), (e), (f), and (g) are the biases simulated with lateral boundary conditions derived from (b) NCEP/DOE reanalysis 2 (NCEP-R2), (c) ECMWF 40-year reanalysis (ERA-40), (d) ECMWF reanalysis INTERIM (ERA-IN), (e) the Japanese 25-year reanalysis (JRA-25), (f) the equally weighted ensemble mean of the four reanalysis datasets, and (g) the Bayesian model averaging (BMA) ensemble mean of the four reanalysis datasets. All the biases are defined by the departure of RCM simulations from the corresponding large-scale forcing. (a) is the averaged wind field and geopotential height at 850 hPa of the four reanalysis datasets.

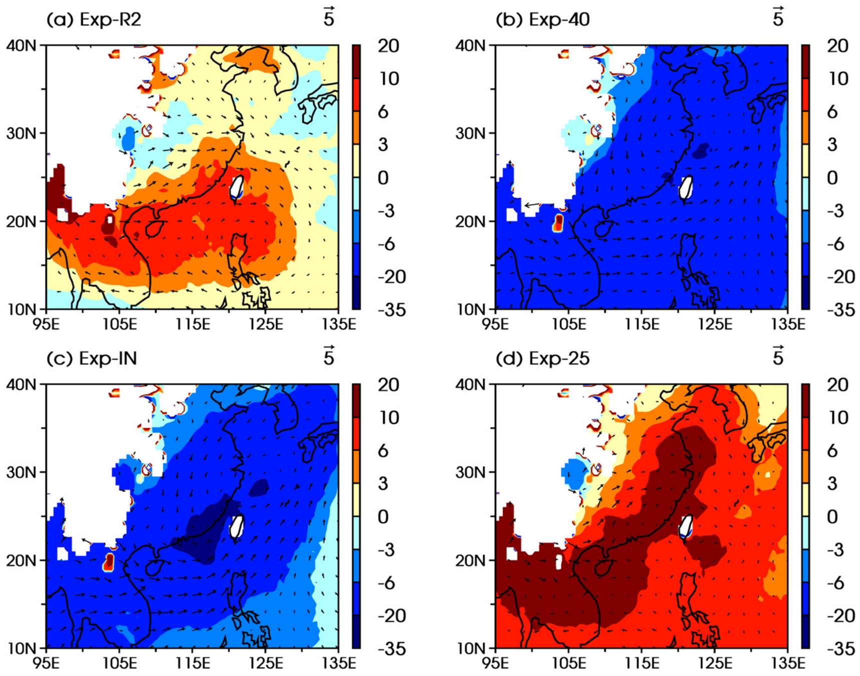

Figure 5 Similar to figure 4, but all the biases are defined by the departure of RCM simulations from the equally weighted ensemble mean of the four reanalysis datasets. Respectively, (a), (b), (c), and (d) are the biases simulated with lateral boundary conditions derived from (a) NCEP/DOE reanalysis 2 (NCEP-R2), (b) ECMWF 40-year reanalysis (ERA-40), (c) ECMWF reanalysis INTERIM (ERA-IN), and (d) the Japanese 25-year reanalysis (JRA-25).

The differences among simulations were observed not only in low-level circulation but also in seasonal mean precipitation. Compared with Exp-R2 and Exp-25, Exp-40 and Exp-IN produced much more precipitation over the Indo-China peninsula and the oceanic region in simulation domain. Exp-40 produced more precipitation in the eastern Yangtze River Basin than did Exp-IN. Exp-40 produced less precipitation in the western Yangtze River Basin than did Exp-IN. Exp-25 simulated more precipitation over the Philippines and adjoining ocean than did Exp-R2 (figures not shown).

Table 1 Spatial correlation coefficients (R) and spatial root mean square error (RMSE) of seasonal precipitation between the observation and Exp-R2, Exp-40, Exp-IN, Exp-25, CTL, and Exp-BMA over land of North China (NC), the Yangtze River Basin (YZ), and South China (SC). Rt is the temporal correlation coefficient of daily precipitation averaged over land of NC, YZ, and SC between the observation and the simulations

R / RMSE / Rt	NC	YZ	SC
Exp-R2	0.71 / 1.65 / 0.49	0.26 / 4.04 / 0.38	0.42 / 4.97 / 0.67
Exp-40	0.60 / 1.47 / 0.25	0.18 / 4.38 / 0.31	0.20 / 6.42 / 0.30
Exp-IN	0.64 / 1.37 / 0.45	0.08 / 4.54 / 0.11	0.12 / 7.79 / 0.39
Exp-25	0.72 / 1.34 / 0.63	0.33 / 4.14 / 0.57	0.41 / 5.28 / 0.49
CTL	0.68 / 1.53 / 0.40	0.10 / 4.96 / 0.39	0.43 / 6.70 / 0.62
Exp-BMA	0.78 / 1.07 / 0.42	0.02 / 3.76 / 0.44	0.48 / 4.63 / 0.52

Model skills in simulating seasonal precipitation are shown in Table 1, which presents the spatial correlation coefficient (R; see the following formula) and spatial root mean square error (RMSE; see the following formula) between the simulation and the rain-gauge observation in three regions over land in China (i.e., North China, the Yangtze River Basin, and South China in figure 3). Among the sensitivity experiments forced by individual reanalysis datasets, Exp-25 had the largest R of 0.72, while Exp-40 had the smallest R of 0.60 over North China. The other experiments had the R values between the R of Exp-25 and Exp-40, respectively, with R values of 0.71 and 0.64 in Exp-R2 and Exp-IN. Over the Yangtze River Basin, all sensitivity experiments forced by individual reanalysis datasets showed different R values, but generally the R was small (0.26 in Exp-R2; 0.18 in Exp-40; 0.08 in Exp-IN; 0.33 in Exp-25) . Only Exp-25 (R=0.33) and Exp-R2 (R=0.26) showed some degree of skills, while Exp-IN showed no skills (R=0.08). Over South China, Exp-R2 had the largest R of 0.42, whereas Exp-IN had the smallest R of 0.12. Exp-40 and Exp-25 had R values of 0.20 and 0.41 respectively.

In terms of RMSE, the results of the sensitivity experiments forced by individual reanalysis datasets were also different. Exp-25 had the smallest RMSE (1.34) while Exp-R2 had the largest RMSE (1.65) over North China. The RMSEs in Exp-40 and Exp-IN were 1.47 and 1.37 respectively. Over both the Yangtze River Basin and South China, the smallest RMSEs were observed from Exp-R2 (4.04; 4.97), while the largest RMSEs were observed from Exp-IN (4.54; 7.79). Exp-40 (4.38; 6.42) had larger RMSEs than Exp-25 (4.14; 5.28) in both the Yangtze River Basin and South China. Generally, however, the RMSEs were observed over the Yangtze River Basin and South China are larger than those over North China, which means the tropical rainfall is difficult to simulate.

Table 1 also shows the temporal correlation coefficient (Rt; see the above formula) of daily precipitation averaged over North China, the Yangtze River Basin, and South China between the simulation and the observation. In North China, Exp-25 (R=0.63) performed best, followed by Exp-R2 (R=0.49). The Rt of Exp-40 and Exp-IN were 0.25 and 0.45 respectively. In the Yangtze River Basin, Exp-25 had the largest Rt of 0.57, while Exp-IN has the smallest Rt of 0.11. Exp-R2 and Exp-40 has Rt of 0.38 and 0.31 respectively. In South China, Exp-R2 had the largest Rt of 0.67 and Exp-40 had the smallest Rt of 0.30. Exp-IN and Exp-25 had the Rt of 0.39 and 0.49 respectively. Thus, Exp-25 performed best in both North China and the Yangtze River Basin.

With the same configuration and model set up, the aforementioned differences among the sensitivity experiments forced by individual reanalysis datasets could only be caused by the different initial condition and the different lateral boundary forcing.

To isolate the main sources of uncertainty, we carried out the sensitivity experiments on the initial condition. We replaced the initial conditions of Exp-R2, Exp-40, Exp-IN, and Exp-JRA with the averaged initial condition of themselves, and the resultant four experiments are referred to as Exp-R2(ctlInit), Exp-40(ctlInit), Exp-IN(ctlInit), and Exp-25(ctlInit), respectively. Figure 6 shows the biases in low-level circulation of these four experiments, which are different from the biases in experiments of Exp-R2, Exp-40, Exp-IN, and Exp-JRA. However, compared with the changes induced by both initial and lateral boundary conditions (e.g., changes from Exp-R2 to CTL; figure 4b to 4f), the changes induced only by initial condition (e.g., changes from Exp-R2 figure 4b to Exp-R2(ctlInit) figure 6a) were minor, which indicates the biases were mainly determined by the lateral boundary forcing.

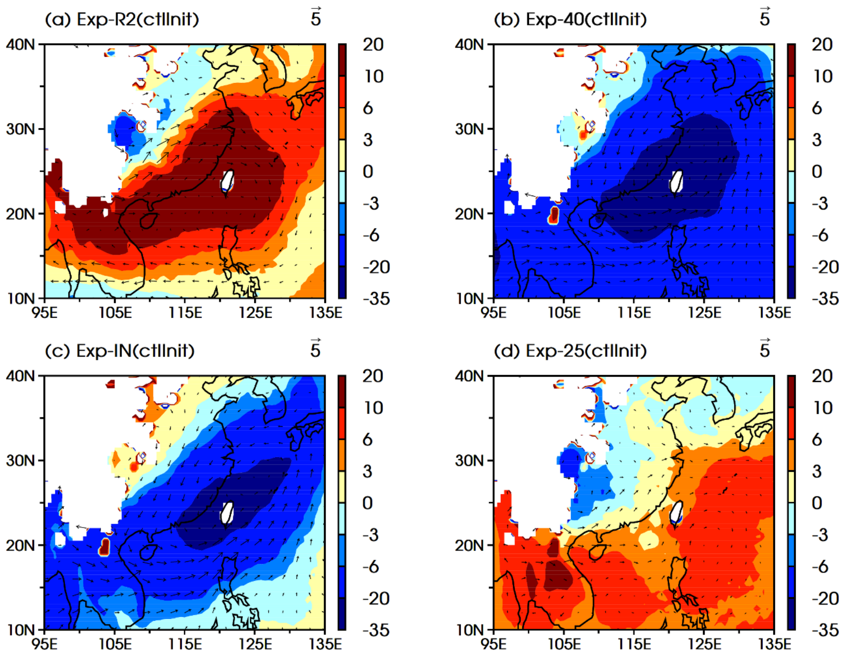

Figure 6 As figure 4, but for sensitivity experiments of Exp-R2(ctlInit), Exp-40(ctlInit), Exp-IN(ctlInit), and Exp-25(ctlInit). All the biases are defined by the departure of RCM simulations from the corresponding large-scale forcing.

Thus, to sharpen up our foci, we only investigated the error sources from the lateral boundary forcing. As found by Wang and Yang (2008) and Yang et al. (2011), here, the uncertainties in humidity fields of the lateral boundary forcing might also be the most important reason for the discrepancies. A detailed analysis is presented in the next section.

5. The source of the biases

To determine the forcing field that most likely to result in the large discrepancies in the last section, we investigated the relative differences among the forcing fields: horizontal wind speed, geopotential height, absolute humidity, and temperature of the four reanalysis datasets. The absolute humidity is computed from the simulated humidity fields at the most outer margin of the buffer zone, and is equal to the value of the forcing field.

We used the spatial average of noise-to-signal ratio (NSR; the spatial average of the inverse of signal-to-noise ratio; see the following formula), on each side of the lateral boundaries from 1000mb up to 100mb in JJA to determine the relative differences of a variable among the four reanalysis datasets. As an example, for absolute humidity at the western boundary, we first calculated the JJA mean absolute humidity for the four reanalysis datasets. Then, for each point on the western boundary, we calculated the noise-to-signal ratio from the four JJA mean absolute humidity. Finally, the NSR was defined as the spatial average of the noise-to-signal ratio at the western boundary. Larger (smaller) values of NSR indicate that the relative differences of a variable among the four reanalysis datasets were larger (smaller). Near a wind shear, the u or v component of the horizontal wind becomes very small, leading to a huge NSR value that cannot reflect the actual differences in winds among the four reanalysis datasets. Therefore, wind speed was used to measure the wind differences instead of u or v.

Table 2 shows that absolute humidity had the largest values of NSRs at all lateral boundaries, which means that the differences in absolute humidity was most likely to be the key factor resulting in the large discrepancies in between the experiments forced by individual reanalysis datasets. Unlike the western, eastern, and southern lateral boundaries, although the NSR value (0.17) was large at the northern boundary, it didn’t mean the relative differences was large because the spatial average of the mean absolute humidity (i.e., an approximation of the signal in NSR; see the following formula) was the minimal (i.e., 2.66). Thus only at the western, eastern, and southern boundaries, the uncertainties in humidity field could induce the large discrepancies in experiments forced by individual reanalysis datasets.

Table 2 Spatial average of noise-signal ratio (NSR) of large-scale forcing fields at the western, eastern, southern, and northern lateral boundaries. The symbols WS, z, a, and T represent wind speed, geopotential height, absolute humidity, and air temperature, respectively. The spatial average of the signal (mean) of absolute humidity is also shown

NSR/mean	WS	z	a	T
West	0.07	0.00	0.17/5.53	0.00
East	0.04	0.00	0.12/5.94	0.00
South	0.06	0.01	0.14/7.00	0.00
North	0.04	0.00	0.17/2.66	0.00

It is difficult for both GCM outputs and reanalysis datasets to diminish the uncertainties in the humidity field, especially on upper levels. To date, the observed humidity is poor both in quantity and quality. Quality of balloons data is poor at very high and very low humidity, and its varieties depend on the instruments and practices between countries, which sometimes makes the data interpretation difficult (Elliott and Gaffen 1991). Radiosonde data is limited at high altitude and is lacking over remote oceanic regions. Satellite data has low-resolution vertical profiles and doesn't provide water vapor data in all weather conditions (Prabhakara et al. 1985; Rind et al. 1993; Rocken et al. 1993). Thus, it is not necessary to surprise there are considerable difference in the moisture field among the four reanalysis datasets.

In order to determine where the humidity field had the large differences, the standard deviation ($std_{i,l}$) of JJA mean absolute humidity of the four reanalysis datasets at the western, southern, and eastern lateral boundaries below 300 hPa are shown in figure 7. The large humidity differences at the western boundary were observed at the boundary layer and the middle atmosphere over the Bay of Bengal. At the southern boundary, the large humidity differences existed at the east side of the boundary. At the eastern boundary, the large humidity differences existed in the boundary layer and the low-level atmosphere over the Philippine Sea. Although the vertical distribution of the humidity differences varied from place to place, but it was clear that almost all the large differences of humidity pronounced over ocean, which is in agreement with the findings in Wang and Yang (2008) and Yang et al. (2011). We will reduce the large uncertainties in humidity field of the lateral boundary forcing over ocean through BMA method in the next section.

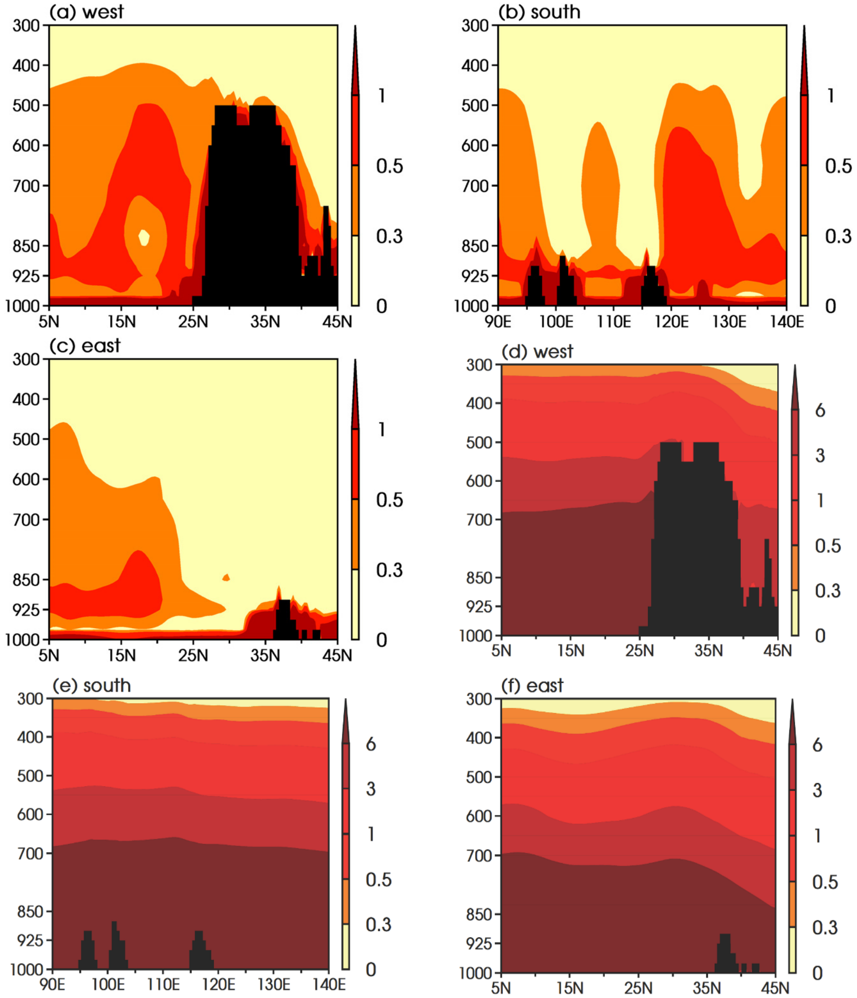

Figure 7 The standard deviation ($std_{i,l}$; g m-3) of JJA mean absolute humidity of the large-scale reanalysis forcing of NCEP-R2, ERA-40, ERA-IN, and JRA-25 at the western (a), southern (b), and eastern (c) lateral boundaries below 300 hPa. (d), (e) and (f) are the means (g m-3) of JJA absolute humidity of the large-scale reanalysis forcing of NCEP-R2, ERA-40, ERA-IN, and JRA-25 at the western, southern, and eastern lateral boundaries below 300 hPa. Black color represents topography.

6. Application of BMA

BMA is a statistical approach to generate the ensemble mean that outperforms any single ensemble member (Hoeting et al. 1999). Raftery et al. (2005) successfully applied BMA to a 48-hour regional weather forecast on surface temperature and sea level pressure. Min et al. (2007) carried out a climate change study based on BMA method. Duan et al. (2007) applied BMA to hydrologic prediction and found that BMA prediction is generally superior to the best individual prediction. Sloughter et al. (2007, 2010) applied BMA to precipitation and wind speed forecasting. Different from other multi-model ensemble methods, BMA provides a more realistic description of the predictive uncertainty that accounts for both between-model variances and in-model variances. In this study, we applied the BMA method to the humidity field of the lateral boundary forcing in dynamic downscaling of the East Asian summer monsoon performed with WRF model. The approach is briefly described as follows.

Because all the underlying models of the four reanalysis datasets depicted the atmospheric behaviors, the water vapor path of the four reanalysis datasets could be considered as estimations of the truth of the water vapor path in the atmosphere. The posterior probability $p(M_k^w | O^w)$ was the probability of the water vapor path simulated by the k-th reanalysis model conditional on the observed water vapor path, which reflected how well the reanalysis dataset mimicked the observed water vapor path at the given places (locations indicated by the blue points in figure 3). The sum of those posterior probabilities was equal to one, thus they could be regarded as a set of weights to measure the skills of reanalysis background models. Because the water vapor path is the vertical integration of the humidity, thus the weights obtained from two-dimensional water vapor path could be used to weight humidity in three dimensions. Then the probability of BMA ensemble mean of the humidity near the whole lateral boundary region was the weighted sum of the probability of the humidity from the four reanalysis datasets:

$$p(h) = \sum_{k=1}^{4} w_k p(h | M_k),$$

where h is the BMA ensemble mean of humidity field, $p(h|M_k)$ is the probability of simulated humidity based on the k-th reanalysis model, the weight w_k is the posterior probability $p(M_k^w|O^w)$.

The observed training data was the water vapor path of HOAPS-3 twice a day from 00Z April 22 through 18Z August 31 in 1998 at the locations indicated by the blue points in figure 3. The data captured water vapor path right near the lateral boundary over the Bay of Bengal, the South China Sea, the Philippine Sea, and the western North Pacific, where the humidity differed considerably among reanalysis datasets and led to the large discrepancies in dynamic downscaling of East Asian summer monsoon.

To calculate the weights (posterior probabilities), the humidity fields of reanalysis datasets were horizontally interpolated to the points in 17 vertical levels that geographically overlaid the blue points in figure 3. The satellite observed field is the water vapor path. It is the vertical summation of water vapor contained in the entire atmosphere. It is a two-dimensional field. Thus, we vertically integrated the three-dimensional water vapor fields of the four reanalysis datasets to obtain the two-dimensional fields that were comparable to the satellite observation.

We calculated the weights through the Expectation–Maximization algorithm (e.g. Hoeting et al. 1999 and Duan et al. 2007). Usually we use the log-likelihood function to maximize the likelihood function instead of using the likelihood function itself. Denote:

$$\theta = [\{w_k, \sigma_k, k = 1,2,\ldots,K\}],$$

the log-likelihood function can be approximated as:

$$l(\theta) = \log\left(\sum_{k=1}^{k} w_k \bullet p_k(y|f_k)\right),$$

Obviously, it is impossible to solve analytical solution of θ and the numerical computational method must be used. Following the recommendation of Raftery et al. (2005), we used the Expectation–Maximization algorithm to calculate the maximum of $l(\theta)$. The Expectation–Maximization algorithm treats the maximum likelihood issue as a "missing data" problem. The "missing data" is a virtual variable without any real physical meaning but a variable introducing mathematically to solve the mathematic problem. In this study, a virtual variable $z_{k,t}$ is introduced. If the ensemble member of the $k-\text{th}$ reanalysis is the best estimation at time t, $z_{k,t}=1$; otherwise $z_{k,t}=0$. At any given time t, there is only one $z_{k,t}$ equal to 1 and all the others are equal to zero. The Expectation–Maximization algorithm alternates between the expectation step and the maximization step. It starts with an initial guess, $\theta^{(0)}$, for parameter θ. In the expectation step, $z_{k,t}$ is estimated given the current guess of θ. In the maximization step, θ is estimated given the current values of the $z_{k,t}$. The Expectation–Maximization steps are repeated until certain convergence criteria are satisfied. For a detailed description of the Expectation–Maximization algorithm, readers are referred to McLachlan and Krishnan (1997).

To ensure that the distribution of the water vapor path approximated normality, a Box–Cox transformation (Box and Cox 1964) was used to preprocess the water vapor path of the observation and the four reanalysis datasets before utilizing the Expectation–Maximization algorithm. This power transformation takes the following form:

$$z=\begin{cases}\dfrac{y^{\lambda}-1}{\lambda}, & \lambda\neq 0\\ \log(y), & \lambda=0\end{cases},$$

where y is the observation or reanalysis datasets and z is the transformed variable. The same transformation parameter λ for the observation and reanalysis datasets was inferred from the Maximum Likelihood method. The Gaussian assumption is made for lessoning computational cost and BMA scheme can be applied by assuming other probability distributions. Statistical techniques such as Markov Chain Monte Carlo (MCMC) method is capable of simulating any complex probability distribution.

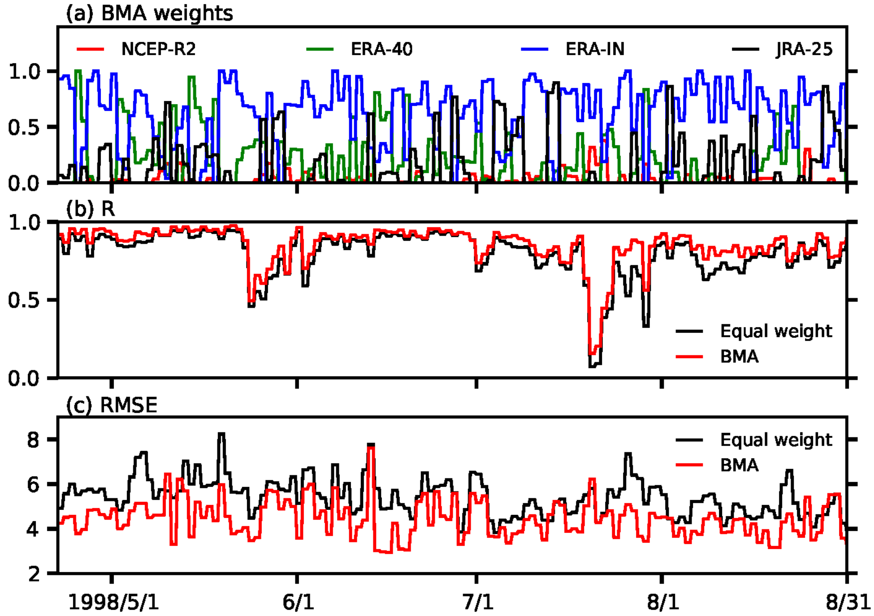

Figure 8 (a) is the Bayesian model averaging (BMA) weights of the water vapor path of NCEP-R2 (red), ERA-40 (green), ERA-IN (blue), and JRA-25 (black) calculated from satellite-observed training data HOAPS-3 at the locations indicated by the blue points in figure 3. (b) and (c) are respectively the correlation coefficients (R) and root mean square error (RMSE) of water vapor path of equally weighted ensemble mean (black) and BMA ensemble mean (red) of the four reanalysis datasets relative to HOAPS-3.

Figure 8a shows the weights of the four reanalysis datasets with the same temporal resolution as the HOAPS-3 in 12 hours intervals at 00z and 12z. The weights at 06z (18z) took their former values at 00z (12z) because of the necessity of the 6-hourly interval of the lateral boundary forcing. The weights of ERA-IN had the most chances being the largest ones, which meant that the water vapor path of ERA-IN was closest to that of HOAPS-3 among the four reanalysis datasets, while the weights of NCEP-R2 had the most chances being the smallest ones. The weights of EAR-40 were more pronounced than the weights of JRA-25 around in the early integration stage.

Figure 8 b and 8 c compare the water vapor path between the equally weighted ensemble mean and the BMA ensemble mean of the four reanalysis datasets based on the observation. Relative to HOAPS-3, the R of water vapor path of the BMA ensemble mean was higher than that of the equally weighted ensemble mean at almost all the times, the RMSE of water vapor path of the BMA ensemble mean was significantly reduced compared with that of the equally weighted ensemble mean at almost all the times. The humidity obtained from BMA ensemble method is controlled by the individual vapor transfer equation in the model, thus the optimal humidity will not cause the inconsistency with other variables. Forced by the BMA ensemble mean whose water vapor path was closer to HOAPS-3 than that of the equally weighted ensemble mean, what happened in the WRF model will be stated in the next section.

7. Improved simulations

The physical parameterization schemes used in the background models that produced NCEP-R2, ERA-40, ERA-IN, and JRA-25 are different. We assume that the systematic errors obtained from relatively independent model parameterization schemes are random. Thus, an ensemble mean of two or more reanalysis datasets would potentially reduce the uncertainties by canceling out random errors. Uncertainty arising from model parameterization schemes is also one of the major sources of errors in dynamic seasonal prediction. To alleviate prediction errors arising from model physical parameterization scheme, the multi-model ensemble climate prediction has been developed (e.g., Krishnamurti et al. 1999). It was shown that the ensemble climate prediction of global models from different centers yields better results than any individual prediction (e.g. Kalnay and Ham 1989; Palmer et al. 2000; Shukla et al. 2000; Wang et al. 2004). The idea behind the multi-model ensemble is the promise that if the model parameterization scheme are independent of each other, the uncertainty-induced errors in each model may be random in nature; thus, an average approach may reduce the prediction errors induced by the model parameterization schemes. Meanwhile, multi-model ensemble methods can also decrease the uncertainties contained in the initial conditions. Similarly, using a multi-reanalysis-datasets ensemble mean as the lateral boundary forcing, the RCM produces better results than any experiment forced by individual reanalysis dataset

(Wang and Yang 2008 and Yang et al. 2011).

In this study, the equally weighted ensemble mean of horizontal winds, geopotential height, temperature, and humidity from the NCEP-R2, ERA-40, ERA-IN, and JRA-25 reanalysis datasets was used as the lateral boundary forcing in the CTL experiment. Another sensitivity experiment, Exp-BMA, was similar to the CTL but the ensemble mean of the humidity field was based on the BMA method. The setup of these experiments was the same as the formers.

The CTL and Exp-BMA were observed to be superior in low-level circulation. Figures 4f and 4g show model biases of 850-hPa JJA mean geopotential height and horizontal winds in CTL and Exp-BMA respectively. Compared with the experiments forced by individual reanalysis datasets in figures. 4b-e, the CTL (figure 4f) dramatically reduced circulation biases. The CTL only slightly underestimated the geopotential height over the East China Sea (with a cyclone wind bias) and western South China, and only overestimated the geopotential height over Laos. The improvement in the CTL forced by the equally weighted ensemble forcing agrees with the findings in Wang and Yang (2008) and Yang et al. (2011).

Surprisingly, Exp-BMA (figure 4g) further and significantly decreased the underestimated biases of geopotential height in the CTL. The underestimated geopotential height (smaller than −3 m) existed only over several small areas without organized pattern in wind biases, although the area of overestimated geopotential height slightly increased over Indo-China peninsular. Compared with the CTL, the further improvement seen in Exp-BMA was totally benefitted from the BMA ensemble method applied to the lateral boundary humidity field. Thus constrained by the observed humidity even in 2 dimensions, i.e. water vapor path over ocean, the lateral boundary forcing would force the model results with much less biases.

The improvements were also observed in seasonal precipitation. Table 1 shows that the CTL had a larger R (0.68) than those of did the Exp-40 (0.60) and Exp-IN (0.64) in North China, but its R was smaller than those of Exp-R2 (0.71) and the R of Exp-25 (0.72). Over South China, the CTL had a larger R (0.43) than those of all experiments forced by individual reanalysis datasets (0.42 in Exp-R2; 0.20

in Exp-40; 0.12 in Exp-IN; 0.41 in Exp-25). Exp-BMA had the largest Rs (0.78 and 0.48) among all experiments in both North China and South China. In the Yangtze River Basin, almost all experiments had no skills in terms of low R, which was probably caused by pattern shift in precipitation. Over all, the CTL was not as good as we expected, but Exp-BMA had better performance.

In terms of RMSE, the CTL had relatively lower skills than those of most experiments forced by individual reanalysis datasets over both of North China (RMSE=1.53) and South China (RMSE=6.70), and also had lower skills than those of all experiments forced by individual reanalysis datasets in the Yangtze River Basin (RMSE=4.96), while Exp-BMA had the highest skills in terms of RMSE in all experiments in three regions, i.e. 1.07 in North China, 3.76 in the Yangtze River Basin, and 4.63 in South China.

Table 1 also shows the temporal correlation coefficient (Rt) of daily precipitation between the simulation and observation averaged over North China, the Yangtze River Basin, and South China. The CTL had better performance than that of Exp-40 (0.40 vs 0.25) in North China, and only had worse performance than that of Exp-25 (0.39 vs 0.57) in the Yangtze River Basin and that of Exp-R2 (0.62 vs 0.67) in South China. Although Exp-BMA did not perform well compared with some experiments, it is better than the CTL in both North China (0.42 vs 0.40) and the Yangtze River Basin (0.44 vs 0.39). Relative to the CTL, The outperformance of Exp-BMA in simulating seasonal precipitation and daily precipitation was benefitted from the BMA ensemble mean of humidity in the lateral boundary forcing.

The results in this study suggest that the CTL forced by the equally weighted ensemble forcing might not reduce the biases in some aspects of the simulations and even sometimes it was worse than the experiments forced by individual reanalysis datasets. However, the BMA ensemble forcing could further reduced the biases in RCM dynamic downscaling, i.e. Exp-BMA outperformed not only the experiments forced by individual reanalysis datasets but also the CTL experiment.

8. Discussion

The uncertainties in a nested RCM mainly come from the lateral boundary forcing (e.g., Giorgi and Bi 2000; Liang et al. 2001; Qian and Liu 2001). Giorgi and Bi (2000) found that biases in nested RCM simulations after the spin-up are essentially dominated by lateral boundary forcing, are generally larger than those induced by initial conditions, and are even larger than those caused by model resolution and physical parameterizations (Vukicevic and Errico 1990; Elía et al. 2008). A well-designed lateral boundary forcing considering geographic location and/or climate condition can improve model performance (Qian and Liu 2001; Liang et al. 2001; Xue et al. 2007). In brief, the quality of lateral boundary forcing is vital to RCM simulation (Gong and Wang 2000; Diaconescu et al. 2007; Dimitrijevic and Laprise 2005).

In simulations of East Asian summer monsoon, Wang and Yang (2008) and Yang et al. (2011) found that the WRF model driven by ERA-40, NCEP-R2, and JRA-25 yields different results. All experiments show large biases in simulating rainfall and atmospheric circulation and the large vapor uncertainties among reanalysis datasets over the Bay of Bengal and the Philippine Sea are identified to be the key factors that induce the large differences. The equal-weight ensemble forcing has the ability of lessoning the uncertainties in large-scale forcing and improving model performance.

However, the experiments performed by Wang and Yang (2008) and Yang et al. (2011), driven by the equal-weight ensemble forcing, did not consider the characteristics of the different reanalysis datasets, especially the humidity fields. Thus, improved simulations can only be achieved in most, not all, of the simulation years. Recently, the optimized ensemble method of Bayesian model averaging (BMA) (Hoeting et al. 1999) has been increasingly used in ensemble prediction (Raftery et al. 2005; Sloughter et al. 2007), climate change projection (Min and Hense 2006), and hydrology prediction study (Duan et al. 2007). BMA is a statistical approach to generating a weighted average of the ensemble members that outperforms any single ensemble member. The weights are estimated according to the performance of individual members in simulating the given training data.

Thus in this study, we applied the BMA method to the humidity field, which has the largest uncertainty among the variables in large-scale forcing fields, to reduce the model biases. Consistent with the results in our previous studies, the experiment forced by the equally weighted ensemble forcing (control or CTL) significantly reduced the biases in simulated circulation, but it only reduced the biases in simulated precipitation in some cases. However, as we expected, the other sensitivity experiment (Exp-BMA) forced by the BMA ensemble forcing reduced the simulation biases not only in circulation field but also in most cases in precipitation compared to the CTL and the experiments forced by individual reanalysis datasets.

This finding calls for cautions in our methodology for verification of the RCMs and calls for attentions to reshape our strategy for validation RCM models. With the launch of A-Train satellites, the access to three-dimensional measurements of moisture and temperature fields over the ocean is expected to lessen the uncertainties in the lateral boundary forcing in RCM simulations. It would be interesting to see the impacts of the three-dimensional satellite observations on the quality of future reanalysis products. Nevertheless, the issues addressed here may provide useful insight for future design of RCM inter-comparison project.

As BMA is a statistical approach to generating a weighted average of the ensemble members that outperforms any single ensemble member. The weights are estimated according to the performance of individual members in simulating the given training data. Thus, BMA method can be used to decrease the uncertainties of the multi-model products of the APCC datasets of global models. The BMA ensemble mean of the global models can be used as the large-scale forcing fields to drive the RCM. This kinds forecast downscaling study forced by the optimal large-scale forcing should be investigated and has broad perspective.

9. Conclusion

Simulations of the 1998 East Asian summer monsoon were carried out using the WRF model forced by four reanalysis datasets (i.e., NCEP-R2, ERA-40, ERA-IN, and JRA-25), their equally weighted ensemble mean, and their BMA ensemble mean. There were large discrepancies in seasonal circulation at 850 hPa, seasonal precipitation, and daily precipitation (figure 4 and Table 1) in the experiments forced by individual reanalysis datasets. Diagnostic analysis revealed that the differences in moisture fields of the large-scale forcing at the eastern, western, and southern boundaries over ocean were responsible for the large discrepancies. The largest moisture uncertainties were found over the Bay of Bengal, which agrees to the findings of Wang and Yang (2008) and Yang et al. (2011).

As expected, the experiment (control) forced by the equally weighted ensemble forcing significantly reduced the biases in simulated circulations, while it only reduced the biases in simulated precipitation compared with some experiments forced by individual reanalysis datasets. It suggests that the use of equally weighted ensemble forcing may not reduce the biases in all cases, which agrees the decadal findings in Yang et al. (2011) that the use of equally weighted ensemble forcing systematically reduces the biases in RCM simulations in most of the years, but not in all years. The reason might be that the quality of the equally weighted ensemble forcing not only depended on climate cases (Yang et al. 2011) because of the invariant weights, but also highly relied on the choice of the ensemble members when ensemble size was small, and unfortunately which was true for reanalysis datasets in these days. Moreover, experiment forced by the incorrectly weighted ensemble forcing might worsen the results forced by individual forcing.

The experiment (Exp-BMA) forced by the BMA ensemble forcing reduced the simulation biases not only in circulation field but also in most cases in precipitation compared to the CTL and the experiments forced by individual reanalysis datasets. In the lateral boundary forcing of Exp-BMA, the weights of humidity field were determined by how well the reanalysis datasets mimicked the observed water vapor path over ocean where the uncertainties in humidity field of the lateral boundary forcing were the leading factor that induced the large discrepancies in experiments forced by individual reanalysis datasets. Those weights changed with time according to the temporal variations of the quality of individual reanalysis dataset based on the observation. Thus, the BMA ensemble forcing could keep the biases minimal along the time, therefore its quality was guaranteed (figure 8b-c).

Limited by availability of three-dimensional observation and the computational resources, this preliminary study was only carried out for simulation of 1998 East Asian summer monsoon and only relied on the two-dimensional observed water vapor path to seek the weights through the BMA method. This type of study should be repeated under different circulation regimes with varying lateral boundary locations, different dynamic core and physical parameterizations of the WRF model, as well as decadal time-scale simulation, to validate the BMA ensemble forcing in reducing the biases in regional climate downscaling. However, as long as the humidity fields of the lateral boundary forcing have large uncertainties, RCM solutions would have large uncertainties. Our additional studies show that a climatological large uncertainty pertaining to moisture fields among the four reanalysis datasets existed in a large area around the lateral boundary location of our model domain (figure not shown). Thus, changing the lateral boundary location or the model setup would only change our results quantitatively. Even changing the simulation year would uncommonly change our results qualitatively. The biases were expected to be further reduced by using three-dimensional satellite data including not only humidity but also other fields as the training base of the BMA method.

REFERENCES

Andersson A, Bakan S, Fennig K, Grassl H, Klepp CP, Schulz J (2007) Hamburg Ocean Atmosphere Parameters and Fluxes from Satellite Data - HOAPS-3 - twice daily composite. World Data Center for Climate doi:10.1594/WDCC/HOAPS3_DAILY

Anderson CJ, Arritt RW, Takle ES, Pan Z, Gutowski WJ, Otieno FO, Silva RD, Caya D, Christensen JH, Lu¨thi D, Gaertner MA, Gallardo C, Giorgi F, Hong S-Y, Jones C, Juang H-M, Katzfey JJ, Lapenta WM, Laprise R, Larson JW, Liston GE, McGregor JL, Pielke RA, Roads JO, Taylor JA (2003) Hydrologic processes in regional climate model simulations of the central United States flood of June-July 1993. J Hydrometeor 4:584–598

Anthes RA, Kuo YH, Baumhefner DP, Errico RM, Bettge TW (1985) Predictability of mesoscale atmospheric motions. Contribution to "issues in atmospheric and oceanic modeling". Advances in geophysics, vol 28B. Academic Press, pp 159–202

Arritt RW, Rummukainen M (2011) Challenges in regional-scale climate modeling. Bull Amer Meteor Soc 92:365–368

Beniston M, Stephenson D, Christensen O, Ferro C, Frei C, Goyette S, Halsnaes K, Holt T, Jylhae K, Koffi B, Palutikof J, Schoell R, Semmler T, Woth K (2007) Future extreme events in European climate: an exploration of regional climate model projections. Clim Change 81(s1):71

Betts, AK (1986) A New Convective Adjustment Scheme .1. Observational and Theoretical Basis. Quarterly Journal of the Royal Meteorological Society, 112:677-691.

Betts AK, Miller MJ (1986) A New Convective Adjustment Scheme .2. Single Column Tests Using Gate Wave, Bomex, Atex and Arctic Air-Mass Data Sets. Quarterly Journal of the Royal Meteorological Society, 112:693-709.

Bhaskaran B, Jones RG, Murphy JM, Noguer M (1996) Simulations of the Indian summer monsoon using a nested regional climate model: Domain size experiments. Climate Dyn 12:573–587

Box GEP, Cox DR (1964) An analysis of transformations. Journal of the Royal Statistical Society, Series B, 26:211-252

Chen F, Dudhia J (2001) Coupling an advanced land surface-hydrology model with the Penn State-NCAR MM5 modeling system. Part I: model implementation and sensitivity. Mon Wea Rev 129:569–585

Chen S-H, Sun W-Y (2002) A one-dimensional time dependent cloud model. J Meteor Soc Jpn 80:99–118

Christensen JH, Machenhauer B, Jones RG, Schar C, Ruti PM, Castro M, Visconti G (1997) Validation of present-day regional climate simulations over Europe: LAM simulations with observed boundary conditions. Climate Dyn 13:489–506

Curry JA, Lynch AH (2002) Comparing arctic regional climate models. Eos Trans Am Geophys Union 83:87

Davies HC, Turner RE (1977) Updating prediction models by dynamical relaxation: An examination of the technique. Quart J Roy Meteor Soc 103:225–245

Dee DP, Uppala SM, Simmons AJ, Berrisford P, Poli P, Kobayashi S, Andrae U, Balmaseda MA, Balsamo G, Bauer P, Bechtold P, Beljaars ACM, van de Berg L, Bidlot J, Bormann N, Delsol C, Dragani R., Fuentes M, Geer AJ, Haimberger L, S. Healy SB, Hersbach H, Hólm EV, Isaksen L, Kållberg

P, Köhler M, Matricardi M, McNally AP, Monge-Sanz BM, Morcrette JJ, Park BK, Peubey C, de Rosnay P, Tavolato C, Thépaut N, Vitart F (2011) The ERA-Interim reanalysis: configuration and performance of the data assimilation system. Quart J R Meteorol Soc 137:553-597

Diaconescu EP, Laprise R, Sushama L (2007) The impact of lateral boundary data errors on the simulated climate of a nested regional climate model. Climate Dyn 28:333–350

Dickinson RE, Errico RM, Giorgi F, Bates GT (1989) A regional climate model for western United States. Clim Change 15:383–422

Dimitrijevic M, Laprise R (2005) Validation of the nesting technique in a regional climate model and sensitivity tests to the resolution of the lateral boundary conditions during summer. Climate Dyn 25:555-580

Ding Y, Liu Y (2001) Onset and the evolution of the summer monsoon over the South China Sea during SCSMEX field experiment in 1998. J Meteor Soc Jpn 79:255–276

Douville H, Chauvin F, Broqua AH (2001) Influence of soil moisture on the Asian and African monsoons. Part I: mean monsoon and daily precipitation. J Clim 14:2381-2403

Druyan LM, Feng JM, Cook KH, Xue YK, Fulakeza M, Hagos SM, Konare´ A, Moufouma-Okia W, Rowell DP, Vizy EK, Ibrah SS (2009) The WAMME regional model intercomparison study. Climate Dyn DOI:10.1007/s00382-009-0676-7

Duan Q, Ajami NK, Gao X, Sorooshian S (2007) Multi-Model ensemble hydrologic prediction using bayesian model averaging. Advances in Water Resources 30:1371-386

Dudhia J (1989) Numerical study of convection observed during the winter monsoon experiment using a mesoscale two-dimensional model. J Atmos Sci 46:3077–3107

Dyer AJ, Hicks BB (1970) Flux-gradient relationships in the constant flux layer. Quart J Roy Meteor Soc 96:715-721

Elía R, Caya D, Côté H, Frigon A, Biner S, Giguère M, Paquin D, Harvey R, Plummer D (2008) Evaluation of uncertainties in the CRCM-simulated North American climate. Cliamte Dyn 30:113–132

Elliott WP, Gaffen DJ (1991) On the Utility of Radiosonde Humidity Archives for Climate Studies. Bulletin of the American Meteorological Society 72:1507-1520.

Fernández J, Fita L, García-Díez M, Gutiérrez JM (2010) WRF sensitivity simulations on the CORDEX African domain. European Geosciences Union General Assembly

Fu C-B, Wang S-Y, Xiong Z, Gutowski WJ, Lee DK, Mcgregor J, Sato Y, Kato H, Kim JW, Suh MS (2005) Regional climate model intercomparison project for Asia. Bull Amer Meteor Soc 86:257-266

García-Díez M, Fernández J, Fita L (2011) WRF multi-physics ensemble for the african CORDEX domain. International Conference on the Coordinated Regional Climate Downscaling Experiment - CORDEX

Giorgi F, Bates GT (1989) The climatological skill of a regional model over complex terrain. Mon Wea Rev 117:2325–2347

Giorgi F, Bi X (2000) A study of internal variability of a regional climate model. J Geophys Res 105:29503–29521

Giorgi F, Mearns LO (1999) Introduction to special section: regional climate modeling revisited. J Geophys Res 104:6335–6352

Giorgi F, Shields C (1999) Tests of precipitation parameterizations available in the latest version of the NCAR regional climate model (RegCM) over the continental U.S. J Geophys Res 104:6353-6376

Gong W, Wang W-C (2000) A Regional Model Simulation of the 1991 Severe Precipitation Event over the Yangtze–Huai River Valley, Part II: Model Bias. J Clim 13:93-108

Gustafsson N (2002) Sensitivity of limited area model data assimilation to lateral boundary condition fields. Tellus A 42:109-115

Hoeting JA, Madigan D, Raftery AE, Volinsky CT (1999) Bayesian model averaging: A tutorial. Statistical Science 14:382-417

Hong S-Y, Leetmaa A (1999) An evaluation of the NCEP RSM for regional climate modeling. J Clim 12:592–609

Intergovernmental Panel on Climate Change, Climate Models-Projections of Future Climate, pp.285-358, Chap. 6, 1995 IPCC Clim. Change Rep., Cambridge University Press, New York, 1996.

Intergovernmental Panel on Climate Change, Regional Climate Information-Evaluation and Projections, pp.610, Chap. 10, 2001 IPCC Clim. Change Rep., Cambridge University Press, New York, 2001.

Jacob D, Podzun R (1997) Sensitivity studies with the regional climate model REMO. Meteor Atmos Phys 63:119–129

Janjic ZI (1994) The Step-Mountain Eta Coordinate Model - Further Developments of the Convection, Viscous Sublayer, and Turbulence Closure Schemes. Monthly Weather Review 122:927-945

Janjic ZI (2000) Comments on "development and evaluation of a convection scheme for use in climate models". J Atmos Sci 57:3686

Jones RG, Murphy JM, Noguer M (1995) Simulation of climate change over Europe using a nested regional-climate model. Part I: assessment of control climate, including sensitivity to location of boundaries. Q J R Meteor Soc 121:1413–1449

Kalnay E (1996) The NCEP/NCAR 40-Year Reanalysis Project, Bull Amer Meteor Soc 77:437–471

Kanamitsu M, Ebisuzaki W, Woollen J, Yang S-K, Hnilo JJ, Fiorino M, Potter GL (2002) NCEP-DOE AMIP-II Reanalysis (R-2). Bull Am Meteor Soc 83:1631–1643

Klemp JB, Wilhelmson R (1978) The simulation of three-dimensional convective storm dynamics. J Atmos Sci 35

Lacis AA, Hansen JE (1974) A parameterization for the absorption of solar radiation in the earth's atmosphere. J Atmos Sci 31.

Laprise R (1992) The Euler Equations of Motion with Hydrostatic-Pressure as an Independent Variable. Monthly Weather Review 120:197-208

Leung LR, Ghan SJ (1999) Pacific Northwest climate sensitivity simulated by a regional climate model driven by a GCM. Part I: control simulations. J Clim 12:2010–2030

Liang X-Z, Kunkel KE, Samel AN (2001) Development of a regional climate model for US midwest applications. Part I--sensitivity to buffer zone treatment. J Clim 14:4363–4378

Liang X-Z, Li L, Kunkel KE, Ting M, Wang JX (2004) Regional climate model simulation of US precipitation during 1982–2002. Part I: annual cycle. J Clim 17:3510–3529

Lin Y-L, Farley RD, Orville HD (1983) Bulk parameterization of the snow field in a cloud model. J Clim Appl Meteorol 22:1065– 1092

Lorenz EN (1969) The predictability of a flow which possesses many scales of motion. Tellus 21:289–307.

McLachlan GJ, Krishnan T (1997) The EM algorithm and extensions. Wiley; 274pp.

Mearns LO, Gutowski WJ, Jones R Jones R, Leung R, McGinnis S, Nunes A, Qian Y (2009) A regional climate change assessment program for North America. EOS 90:311-312

Min S-K, Daniel S, Andreas H (2007) Probabilistic climate change predictions applying Bayesian model averaging. Phil Trans R Soc, A, 365:2103–2116

Min S-K, Hense A (2006) A Bayesian approach to climate model evaluation and multi-model averaging with an application to global mean surface temperatures from IPCC AR4 coupled climate models. Geophys Res Lett 33:L08708, doi:10.1029/2006GL025779

Miyakoda K, Rosati A (1977) One way nested grid models: The interface conditions and the numerical accuracy. Mon Wea Rev 105:1092–1107

Mlawer EJ, Taubman SJ, Brown PD Iacono MJ, Clough SA (1997) Radiative transfer for inhomogeneous atmosphere: RRTM, a validated correlated-k model for the longwave. J Geophys Res 102(D14), 16,663–16,682, doi:10.1029/97JD00237.

Mohanty UC, Paliwal RK, Tyagi A, John A (1990): Evaluation of a limited area model for short range prediction over Indian region: Sensitivity studies. Mauson, 41:251-256

Noguer M, Jones R, Murphy J (1998) Sources of systematic errors in the climatology of a regional climate model over Europe. Climate Dynamics 14: 691-712.

Noh Y, Cheon WG, Hong SY, Raasch S (2003) Improvement of the K-profile model for the planetary boundary layer based on large eddy simulation data. Bound Layer Meteor 107:401–427

Onogi K, Tsutsui J, Koide H, Sakamoto M, Kobayashi S, Hatsushika H, Matsumoto T, Yamazaki N, Kamahori H, Takahashi K, Kadokura S, Wada K, Kato K, Oyama R, Ose T, Mannoji N, Taira R (2007) The JRA-25 reanalysis. J Meteorol Soc Jpn 85:369–432

Ooyama KV (1990) A Thermodynamic Foundation for Modeling the Moist Atmosphere. Journal of the Atmospheric Sciences 47:2580-2593

Paegle J, Yang Q, Wang M (1997) Predictability in limited area and global models. Meteor Atmos Phys 63:53–69

Pan Z, Christensen JH, Arritt RW, Gutowski Jr WJ, Takle ES, Otieno F (2001) Evaluation of uncertainties in regional climate change simulations. J Geophys Res 106:17735–17751

Paulson CA (1970) The mathematical representation of wind speed and temperature profiles in the unstable atmospheric surface layer. J Appl Meteor 9:857-861

Prabhakara C, Short DA, Volmer BE (1985) El Nino and atmospheric water vapor: Observations from Nimbus 7 SMMR. J Climatol Appl Meteorol, 24:1312-1324.

Qian Y-F, Liu H-Q (2001) On nesting area selection of regional climate models coupled to a global climate model (in Chinese). Chin J Atmos Sci 25:492–502

Raftery AE, Gneiting T, Balabdaoui F, Polakowski M (2005) Using bayesian model averaging to calibrate forecast ensembles. Mon Wea Rev 133:1155-174

Rocken C, Ware R, Vanhove T, Solheim F, Alber C, Johnson J (1993) Sensing Atmospheric Water-Vapor with the Global Positioning System. Geophysical Research Letters 20:2631-2634.

Rutledge SA, Hobbs PV (1984) The Mesoscale and Microscale Structure and Organization of Clouds and Precipitation in Midlatitude Cyclones .12. A Diagnostic Modeling Study of Precipitation Development in Narrow Cold-Frontal Rainbands. Journal of the Atmospheric Sciences 41:2949-2972.

Skamarock WC, Klemp JB (1992) The Stability of Time-Split Numerical-Methods for the Hydrostatic and the Nonhydrostatic Elastic Equations. Monthly Weather Review 120:2109-2127

Skamarock WC, Klemp JB, Dudhia J, Gill DO, Barker DM, Wang W, Powers JG (2005) A description of the advanced research WRF version 2. NCAR tech notes-468 + STR

Sloughter JML, Gneiting T, Raftery AE (2010) Probabilistic Wind Speed Forecasting Using Ensembles and Bayesian Model Averaging. Journal of the American Statistical Association 105:25-35

Sloughter JML, Raftery AE, Gneiting T, Fraley C (2007) Probabilistic quantitative precipitation forecasting using bayesian model averaging. Mon Wea Rev 135:3209-220

Small EE, Giorgi F, Sloan LC (1999a) Regional climate model simulation of precipitation in central Asia: Mean and interannual variability. J Geophys Res 104:6563--6582.

Small EE, Sloan LC, Hostetler S, Giorgi F (1999b) Simulating the water balance of the Aral Sea with a coupled regional climate-lake model. J Geophys Res, 104:6583-- 6602

Stephens GL (1978) Radiation profiles in extended water clouds. Part II: Parameterization schemes. J Atmos Sci 35:2123-2132

Takle ES, Gutowski WJ, Arritt RW, Pan Z, Anderson CJ, da Silva RR, Caya D, Chen S-C, Giorgi F, Christensen JH, Hong S-Y, Juang H-M, Katzfey J, Lapenta WM, Laprise R, Liston GE, Lopez P, McGregor J, Pielke RA, Roads JO (1999) Project to intercompare regional climate simulations (PIRCS): Description and initial results. J Geophys Res 104:19443–19461

Tao WK, Simpson J, Mccumber M (1989) An Ice Water Saturation Adjustment. Monthly Weather Review 117:231-235

Thompson PD (1957) Uncertainty of initial state as a factor in the predictability of large scale atmospheric flow patterns. Tellus 9:275–295

Uppala SM, Kallberg PW, Simmons AJ, Andrae U, da Costa Bechtold V, Fiorino M, Gibson JK, Haseler J, Hernandez A, Kelly GA, Li X, Onogi K, Saarinen S, Sokka N, Allan RP, Andersson E, Arpe K, Balmaseda MA, Beljaars ACM, van de Berg L, Bidlot J, Bormann N, Caires S, Chevallier F, Dethof A, Dragosavac M, Fisher M, Fuentes M, Hagemann S, Ho´lmE, Hoskins BJ, Isaksen L, Janssen PAEM, Jenne R, McNally AP, Mahfouf J-F, Morcrette J-J, Rayner NA, Saunders RW, Simon P, Sterl A, Trenberth KE, Untch A, Vasiljevic D, Viterbo P, Woollen J (2005) The ERA-40 re-analysis. Q J Roy Meteor Soc 131:2961–3012

van Lipzig (1999) The surface mass balance of the Antarctic ice sheet, a study with a regional atmospheric model, Ph. D. thesis, Utrecht University, 154 pp.

Vukicevic T, Errico RM (1990) The influence of artificial and physical factors upon predictability estimates using a complex limited-area model. Mon Weather Rev 118:1460–1482

Wang B, Kang I-S, Lee J-Y (2004) Ensemble simulations of Asian– Australian monsoon variability by 11 AGCMs. J Clim 17:803–818

Wang B, Yang H-W (2008) Hydrological issues in lateral boundary conditions for regional climate modeling: simulation of east asian summer monsoon in 1998. Clim Dyn 31:477–490

Webb EK (1970) Profile relationships: The log-linear range, and extension to strong stability. Quart J Roy Meteor Soc 96:67-90

Wicker LJ, Skamarock WC (2002) Time-splitting methods for elastic models using forward time schemes. Monthly Weather Review 130:2088-2097

Wu W, Lynch AH, Rivers A (2005) Estimating the uncertainty in a regional climate model related to initial and lateral boundary conditions. J Clim 18:917–933

Xie P, Arkin PA (1996) Global precipitation: A 17-year monthly analysis based on gauge observations, satellite estimates, and numerical model outputs. Bull. Amer. Meteor. Soc., 78, 2539–2558.

Xue Y, Vasic R, Janjic Z, Mesinger F, Mitchell KE (2007) Assessment of dynamic downscaling of the continental U.S. Regional climate using the eta/ssib regional climate model. J Clim 20:4172–4193

Yang H-W, Wang B, Wang B (2011) Reduction of systematic biases in regional climate downscaling through ensemble forcing. Clim Dyn DOI 10.1007/s00382-011-1006-4

Yatagai A, Arakawa O, Kamiguchi K, Kawamoto H, Nodzu MI, Hamada A (2009) A 44-year daily gridded precipitation dataset for Asia based on a dense network of rain gauges. SOLA 5:137–140. doi:10.2151/sola.2009-035

Zhong Z (2006) A possible cause of a regional climate model's failure in simulating the east Asian summer monsoon. Geophys Res Lett 33:L24707. doi:10.1029/2006GL027654

APCC TECHNICAL REPORT 2011-01

- Interannual Variability of the Western North Pacific Summer Monsoon
- Reduction Biases in Regional Climate Downscaling
- Typhoon Activity in the North West Pacific Region

APEC Climate Center

12, Centum 7-ro, Haeundae-gu, Busan 612-020,
Republic of Korea
Tel: +82-51-745-3900 Fax: +82-51-745-3949
www.apcc21.org

비매품
94500
9 788997 333165
ISBN 978-89-97333-16-5
ISBN 978-89-97333-15-8 (세트)